

Realization of 2D metals at the ångström thickness limit

<https://doi.org/10.1038/s41586-025-08711-x>

Received: 1 August 2024

Accepted: 29 January 2025

Published online: 12 March 2025

 Check for updates

Jiaojiao Zhao^{1,2,3}, Lu Li^{1,2}, Peixuan Li^{1,2}, Liyan Dai^{1,2}, Jingwei Dong^{1,2}, Lanying Zhou³, Yizhe Wang^{1,2}, Peihang Zhang^{1,2}, Kunshan Ji^{1,2}, Yangkun Zhang^{1,2}, Hua Yu³, Zheng Wei^{1,2}, Jiawei Li^{1,2}, Xiuzhen Li^{1,2}, Zhiheng Huang^{1,2}, Boxin Wang^{1,2}, Jieying Liu³, Yutong Chen³, Xingchao Zhang³, Shuopei Wang³, Na Li³, Wei Yang^{1,2,3}, Dongxia Shi^{1,2,3}, Jinbo Pan^{1,2}, Shixuan Du^{1,2}, Luojun Du^{1,2,✉} & Guangyu Zhang^{1,2,3,✉}

Two-dimensional (2D) metals are appealing for many emergent phenomena and have recently attracted research interests^{1–9}. Unlike the widely studied 2D van der Waals (vdW) layered materials, 2D metals are extremely challenging to achieve, because they are thermodynamically unstable^{1,10}. Here we develop a vdW squeezing method to realize diverse 2D metals (including Bi, Ga, In, Sn and Pb) at the ångström thickness limit. The achieved 2D metals are stabilized from a complete encapsulation between two MoS₂ monolayers and present non-bonded interfaces, enabling access to their intrinsic properties. Transport and Raman measurements on monolayer Bi show excellent physical properties, for example, new phonon mode, enhanced electrical conductivity, notable field effect and large nonlinear Hall conductivity. Our work establishes an effective route for implementing 2D metals, alloys and other 2D non-vdW materials, potentially outlining a bright vision for a broad portfolio of emerging quantum, electronic and photonic devices.

Scaling the thickness of a material down to an atomically thin limit can typically give rise to unique physical properties unattainable in its bulk counterpart, as witnessed by recent advances in the realm of 2D materials^{11–15}. Until now, a rich variety of 2D materials—for example, insulating hexagonal boron nitride (hBN), semiconducting MoS₂ and semimetal graphene—have been realized. Most of these 2D materials are limited to vdW layered crystals in which the weak interlayer interactions facilitate the isolation from their bulk, for example, by mechanical exfoliation^{13,14}. Atomically thin 2D metals are highly sought-after materials, which can not only broaden the 2D family beyond 2D vdW layered materials but also promote a variety of theoretical, experimental and technological advances, such as new quantum optical effects, topological edge states, superconductivity, metallic ferroelectricity, quantum Griffiths singularity, superior nonlinearity, efficient catalysis and all-metallic transistors^{1–6,10,16–18}.

Unlike vdW layered materials, non-vdW materials such as metals are highly symmetric and strongly bonded, thus their 2D forms, especially at the atomically thin limit, are extremely difficult to realize. In principle, a single layer of free-standing metal atoms is thermodynamically unstable. To stabilize a 2D metal structure, we need environmental confinements. The main technical routes include the growth of 2D metal islands on the surfaces of certain materials, including vdW crystals, by molecular beam epitaxy^{2,4,5,7,8,18–22} and the intercalation of 2D metals into interfaces between a 2D vdW layered material and a substrate such as SiC or Ru^{3,23,24}. In both cases, the achieved 2D metals typically feature nanometre-size segmented islands with irregular surfaces or are strongly bonded to substrates thus preventing the investigation of their intrinsic properties and also technological applications.

Moreover, 2D metals grown on the surface are easily oxidized on environmental exposure.

Notably, the conventional hot-pressing method offers a simple route towards thin metal films^{9,25}. This method uses pressing a thick metal in either solid or liquid forms at an elevated temperature for thickness reduction. However, as demonstrated previously, the hot-pressed metal films fall on a few-nm thickness at the minimum, far from the atomically thin limit (please refer to Supplementary Table 1 for more details). Here we demonstrate a convenient, universal vdW squeezing method for the production of large-scale 2D metals at the ångström-scale thickness by two rigid vdW anvils and under high pressure. The vdW squeezing can be applied to diverse 2D metal crystals, including Bi, Ga, In, Sn and Pb, suggesting its universality. Being fully encapsulated inside two MoS₂ monolayers, these 2D metals are large, crystalline and environmentally stable. Taking 2D Bi crystals as an example, we investigate their atomic structures and optical and electronic properties in detail. New phonon mode, strongly enhanced electrical conductivity, notable field effect with *p*-type behaviour, and large nonlinear Hall conductivity are observed.

Ångström-thick 2D metals by vdW squeezing

Figure 1a shows the vdW squeezing process. Please also refer to the experimental apparatus in Extended Data Fig. 1. The two opposite anvils for squeezing are cm-scale *c*-face sapphire with single crystalline monolayer MoS₂ (ML-MoS₂) epitaxially grown on its surface²⁶ (see Supplementary Fig. 1). We highlight the importance of using ML-MoS₂ coated sapphire as anvils (Supplementary Fig. 2): (1) the large-scale,

¹Beijing National Laboratory for Condensed Matter Physics and Institute of Physics, Chinese Academy of Sciences, Beijing, China. ²School of Physical Sciences, University of Chinese Academy of Sciences, Beijing, China. ³Songshan Lake Materials Laboratory, Dongguan, China. [✉]e-mail: luojun.du@iphy.ac.cn; gyzhang@iphy.ac.cn

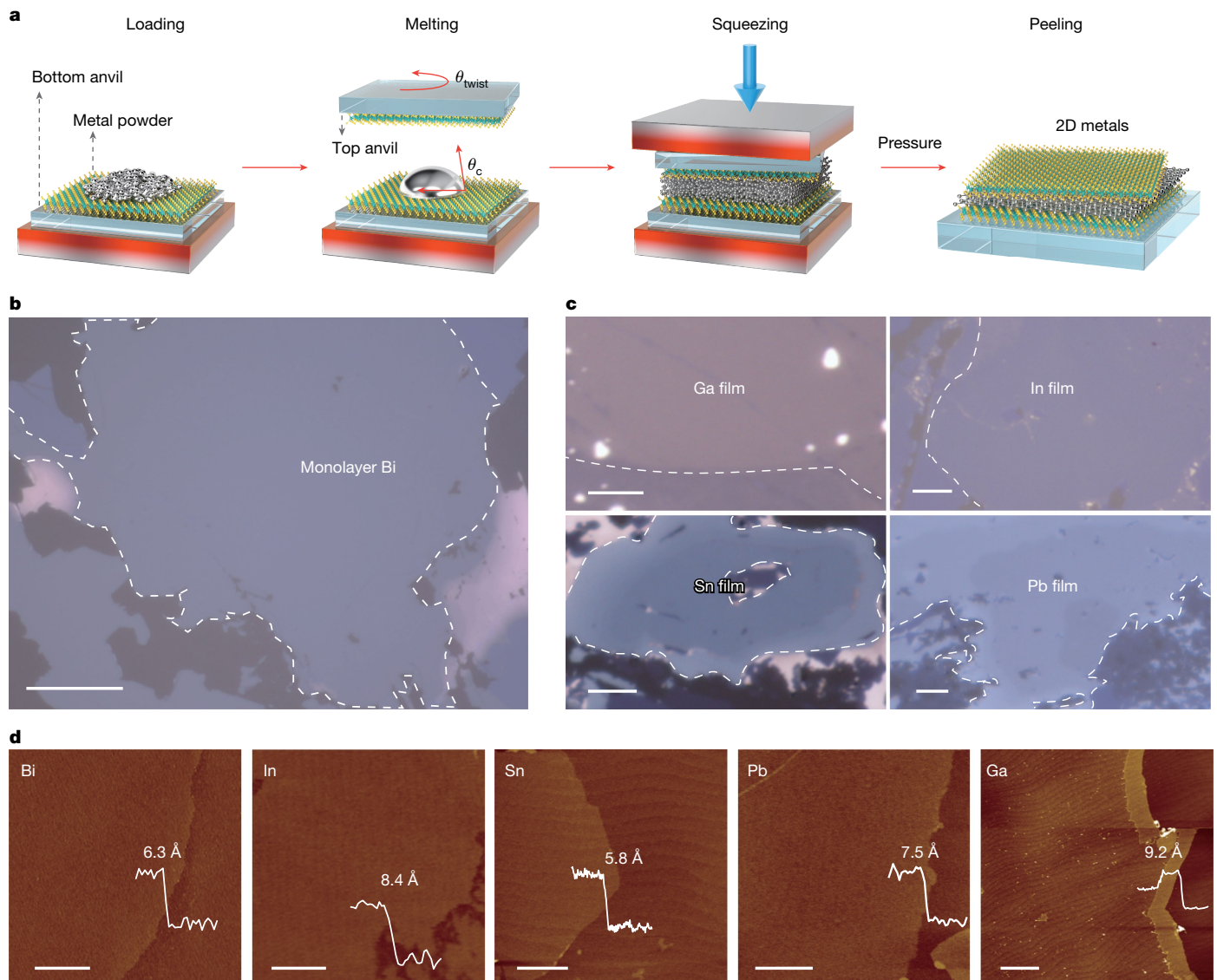


Fig. 1 | vdW squeezing process for 2D metals. **a**, Schematic of vdW squeezing process. **b**, Optical microscope image of monolayer Bi (marked by the white dashed line) fully encapsulated by two MoS₂ monolayers on the anvil. **c**, Optical images of the MoS₂-encapsulated 2D Ga, In, Sn and Pb. **d**, AFM images of

2D metals of Bi, In, Sn, Pb and Ga at the ångström thickness limit. The height profiles are superimposed on each individual image. Scale bars, 20 µm (**b**); 5 µm (**c**); 400 nm, 300 nm, 200 nm, 400 nm and 400 nm (**d**, from left to right).

atomically flat and dangling-bond-free surface of ML-MoS₂/sapphire is critical to thickness uniformity of 2D metals over a large scale; (2) the high Young's modulus of both sapphire (about 430 GPa) and ML-MoS₂ (around 300 GPa) is important to afford the exerted high pressures, enabling 2D metals formed inside the two anvils to approach their ångström thickness limit.

Before squeezing, a certain amount of metal powder is placed on the bottom anvil and then heated until it melts to form a droplet (Fig. 1a, loading and melting). Note that the temperature of the top anvil follows simultaneously. While keeping this temperature unchanged, the two opposite anvils move towards each other until forming a contact. Subsequently, the liquid metal is gradually squeezed by the two anvils for flattening at a high pressure below 200 MPa (to avoid anvil crash). The squeezing process is maintained until the two opposite anvils are cooled down to room temperature and 2D metals are formed eventually (Fig. 1a, squeezing). Unless otherwise specified, the cooling rate is maintained slowly (typically taking a few hours to reach room temperature), facilitating the formation of 2D metals with large sizes (for example, >100 µm) and in the most stable phase. After vdW squeezing,

the as-achieved sapphire/MoS₂/2D-metal/MoS₂/sapphire assembly is loaded out and mechanically cleaved. As the vdW interaction of metal-MoS₂ is larger than that of MoS₂-sapphire, the cleaved interface occurs at the MoS₂/sapphire interfaces, resulting in MoS₂-encapsulated 2D metals on sapphire (Fig. 1a, peeling). Note that the full encapsulation and vdW confinement by ML-MoS₂ are important for the stabilization of the 2D metal structure and also for avoiding exposure to the environment.

Figure 1b shows the optical microscope images of monolayer Bi film successfully obtained by vdW squeezing. Please also refer to a large-scale optical image over an approximately 1 mm² area in Extended Data Fig. 2. Optical microscope images of other 2D metals (that is, Sn, Pb, In and Ga) are shown in Fig. 1c. These 2D metals are reachable in large sizes, for example, about 100 µm for monolayer Bi (as shown in Fig. 1b), two orders of magnitude larger than those reported previously^{2,18,19,27}. The thicknesses of these as-produced 2D metals can all reach the ångström limit, for example, about 6.3 Å for Bi, about 5.8 Å for Sn, about 7.5 Å for Pb, about 8.4 Å for In and about 9.2 Å for Ga, as shown in the atomic force microscope (AFM) images (Fig. 1d).

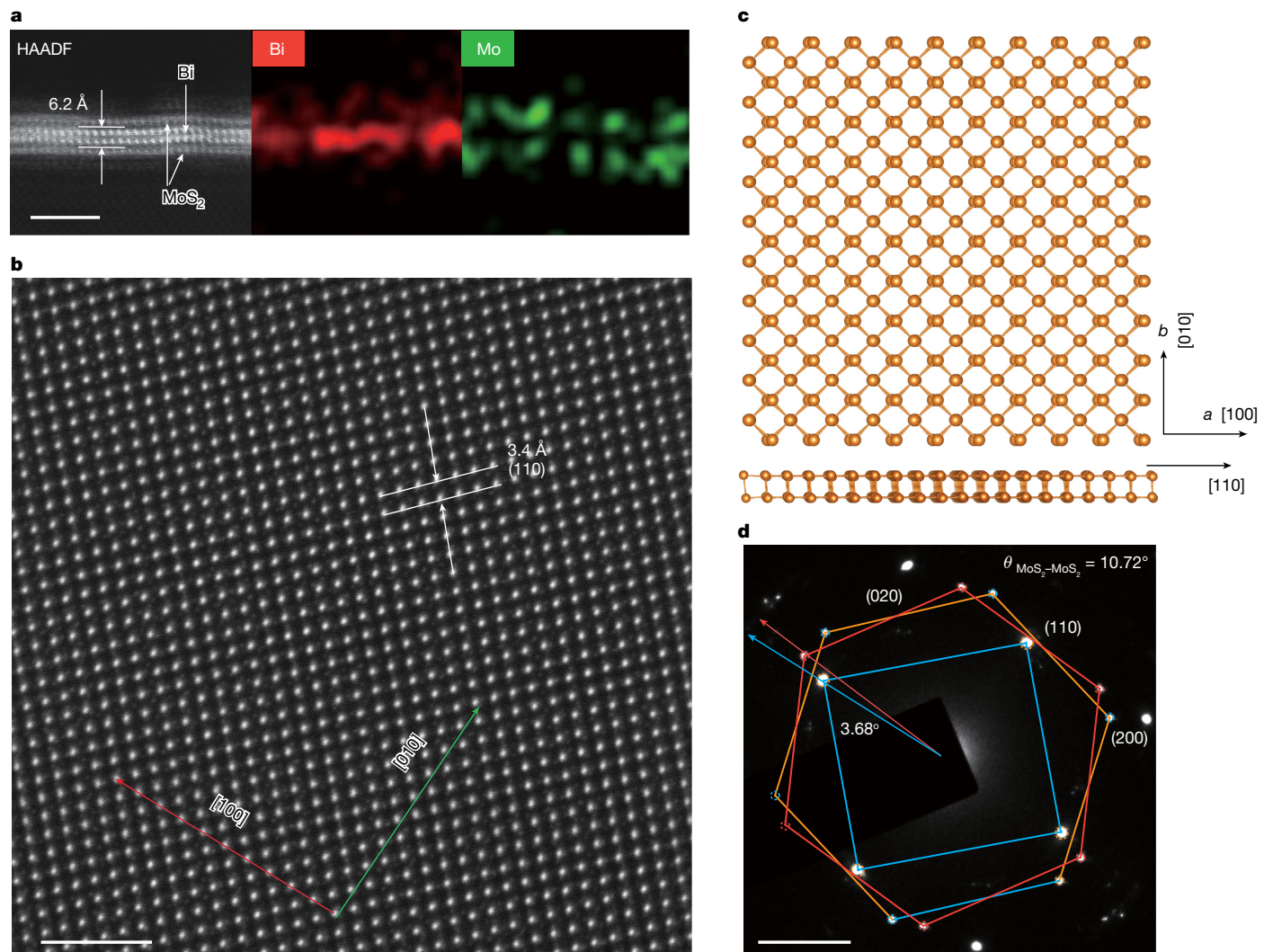


Fig. 2 | Atomic structure of monolayer Bi. **a**, Cross-sectional view HAADF-TEM image (left) and the corresponding EDS mapping of Bi (middle) and Mo elements (right) of a monolayer Bi sample. **b**, Corresponding top view HAADF-TEM image. **c**, Top view (top) and side view (bottom) of the crystal structure of

monolayer Bi. **d**, SAED pattern of an MoS₂-encapsulated monolayer Bi sample. A twist angle of about 10.72° between the top and bottom ML-MoS₂ layer is shown, whereas the inside monolayer Bi is twisted by around 3.68° against one ML-MoS₂ layer. Scale bars, 3 nm (**a**), 2 nm (**b**) and 2 nm⁻¹ (**d**).

The realization of various 2D metals down to ångström thickness shows the universality and advancement of the vdW squeezing methodology. It is worth noting that, a vdW-moulded approach has been demonstrated recently⁹, whereas the thinnest thickness of the as-pressed Bi films is far from the atomically thin limit, for example, about 8 nm, most likely because of the much less rigid and very local design (Supplementary Note 4 and Supplementary Fig. 3).

Atomic structures of monolayer Bi

Below we focus on 2D Bi to demonstrate its excellent physical properties, as it has recently attracted a wide range of theoretical and experimental interests^{2,9,18,19}. Figure 2a shows a cross-sectional scanning transmission electron microscope (STEM) image (left) of the above-mentioned about 6.3-Å-thick 2D Bi encapsulated inside two MoS₂ monolayers. The multiple atom layers, including the top and bottom ML-MoS₂ and middle two Bi atom layers, can be seen with sharply distinguished elements, as shown by the STEM elemental mapping of Bi (middle) and Mo (right). The two Bi atom layers offer a signature of α -phase Bi(110) with one unit cell thickness¹⁸. Therefore, we call this one-unit-cell thick Bi composing two atom layers of Bi as monolayer Bi hereafter^{28,29}. The top-view atomic-resolution high-angle annular

dark-field STEM (HAADF-STEM) image is shown in Fig. 2b. Note that because Bi atoms are much heavier than Mo and S, only Bi atoms can be resolved. The monolayer Bi displays a perfect rectangular lattice, indicating the high crystalline quality. From Fig. 2b, we can extract lattice constants of $a = 5.03 \pm 0.03$ Å and $b = 4.64 \pm 0.03$ Å and the (110) inter-planar spacing of about 3.4 Å (Supplementary Fig. 4). These results confirm that the achieved monolayer Bi is α -phase with unit cell composing two atom layers of Bi (refer to Fig. 2c for the schematic atomic structure), in accordance with recent studies^{2,18}.

Figure 2d shows a typical selected area electron diffraction (SAED) pattern of an MoS₂-encapsulated monolayer Bi sample. Rectangular diffraction spots (marked in blue) of the monolayer Bi can be recognized explicitly, apart from two sets of six-fold-symmetric spots with a twist angle of about 10.72° (marked in red and orange), coming from the top and bottom ML-MoS₂, respectively. From the SAED patterns, we extract the spacing of Bi(110) plane to be about 3.25 Å, matching well with the atomic-resolution STEM results (Fig. 2b). The diffraction patterns of In, Sn and Pb are provided in Extended Data Fig. 3, suggesting a rectangular lattice for In and Sn, and a hexagonal lattice for Pb. We highlight that we have checked the diffraction for more than 50 monolayer Bi samples (Extended Data Fig. 4); all of them show rectangular patterns and thus are α -phase. This matches with our theoretical calculations that

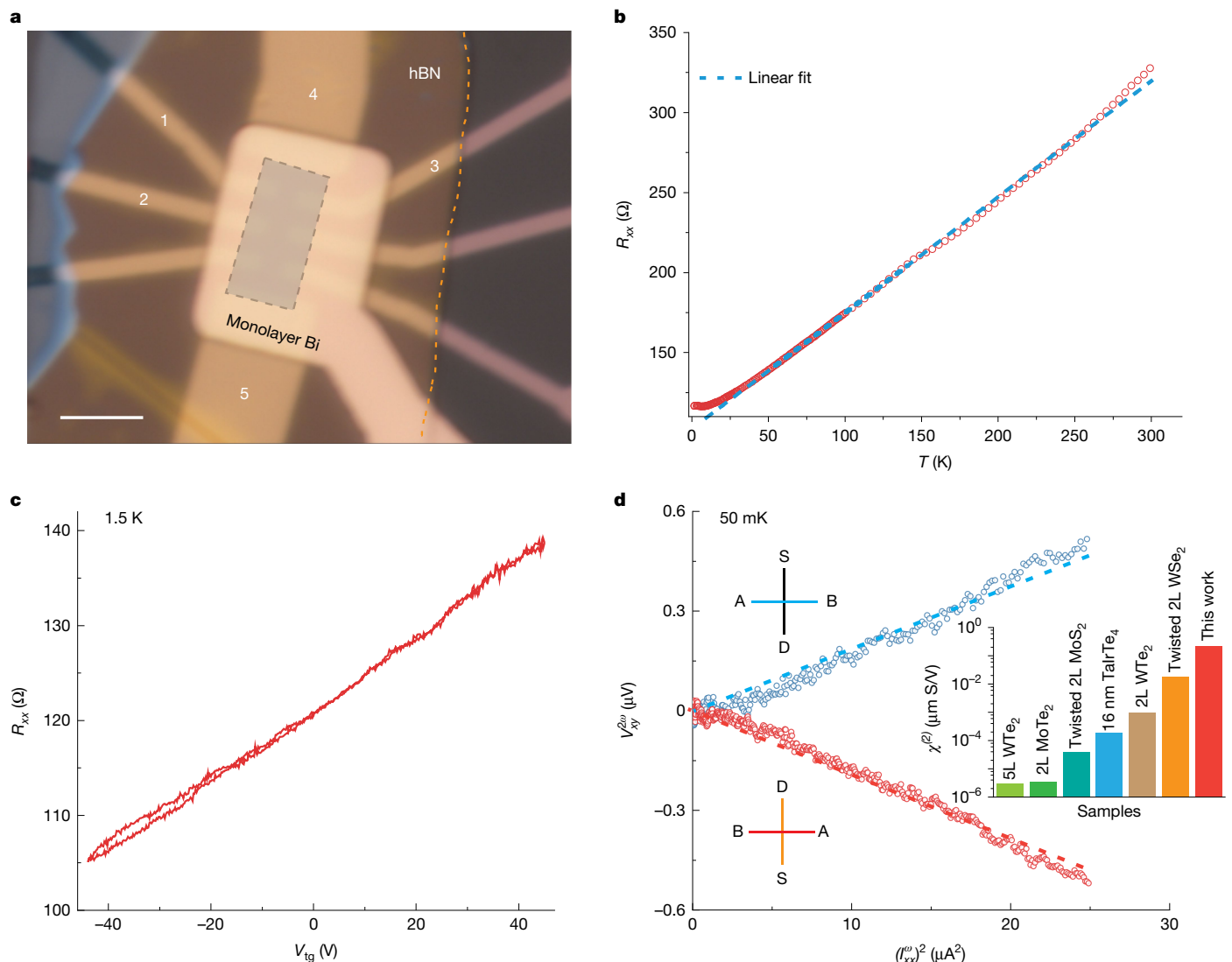


Fig. 3 | Electrical properties of monolayer Bi. **a**, Optical microscope image of a monolayer Bi device with hBN as the top-gate dielectric layer and Au as the contact and top-gate electrodes. Scale bar, 5 μm . **b**, R_{xx} –T curve. **c**, Dual-sweep of R_{xx} as a function of V_{tg} . **d**, Nonlinear Hall voltage $V_{xy}^{2\omega}$ as a function of the square of the driving current $(I_{xx})^2$. The electrode geometries for the forward current

(black) and backward current (red) directions are shown. The current is injected from S to D and the voltage is measured between A and B. The insert chart shows a benchmark comparison of nonlinear Hall conductivity between monolayer Bi with those reported previously with a dominated BCD contribution. The extracted data are from refs. 32–35, 37, 38.

for monolayer Bi encapsulated within two MoS₂ monolayers, α -phase Bi (110) is more stable than β -phase Bi (111) (Extended Data Fig. 5 and Supplementary Note 6).

As mentioned above, the large-size monolayer Bi, for example, more than 100 μm , resulted from the very slow cooling rate during vdW squeezing. A series of SAED characterizations at 20 randomly picked positions across a large-size monolayer Bi is shown in Extended Data Fig. 6, suggesting its single-crystal nature and uniformity. The α -phase and crystallinity are also confirmed by in-plane X-ray diffraction (XRD) measurements (for more details, refer to Extended Data Fig. 7 and Supplementary Fig. 5). We have also carried out experiments by using a much faster cooling rate (Extended Data Fig. 8). The grain sizes of the as-achieved Bi monolayers are much smaller, that is, typically less than 1 μm , and the grain boundaries can be easily distinguished.

Regarding a monolayer Bi inside two MoS₂ monolayers with a certain twist angle $\theta_{\text{MoS}_2-\text{MoS}_2}$, it is fundamentally interesting to see the dependence of the twist angles of monolayer Bi with respect to the top (θ_T) and bottom (θ_B) monolayer MoS₂. Note that $\theta_{\text{MoS}_2-\text{MoS}_2} = \theta_T + \theta_B$. We thus fabricate samples with various $\theta_{\text{MoS}_2-\text{MoS}_2}$ and collect correspond-

ing FFT-transformed reciprocal patterns, as shown in Supplementary Fig. 6. The relationship between $\theta_T + \theta_B$ and $|\theta_T - \theta_B|$ is given in Supplementary Fig. 6g. When the twist angle between two MoS₂ monolayers is small (for example, $\theta_{\text{MoS}_2-\text{MoS}_2} < 15^\circ$), it has a strong influence on the orientation of monolayer Bi, resulting in substantial fluctuations. By contrast, monolayer Bi aligns with one of the two monolayer MoS₂ when $\theta_{\text{MoS}_2-\text{MoS}_2}$ approaches 30°.

Transport properties of monolayer Bi

Owning to the complete encapsulation by monolayer MoS₂, the as-produced monolayer Bi with large size is environmentally stable and presents non-bonded interfaces (Supplementary Fig. 10), facilitating the device fabrication to access the intrinsic transport properties, which were unavailable previously. Figure 3a shows the optical image of an as-fabricated Hall bar device. The top-gate dielectrics and the contact electrodes are hBN and Au, respectively. Note that monolayer MoS₂ would become insulating at cryogenic temperatures and thus does not contribute to electrical transports.

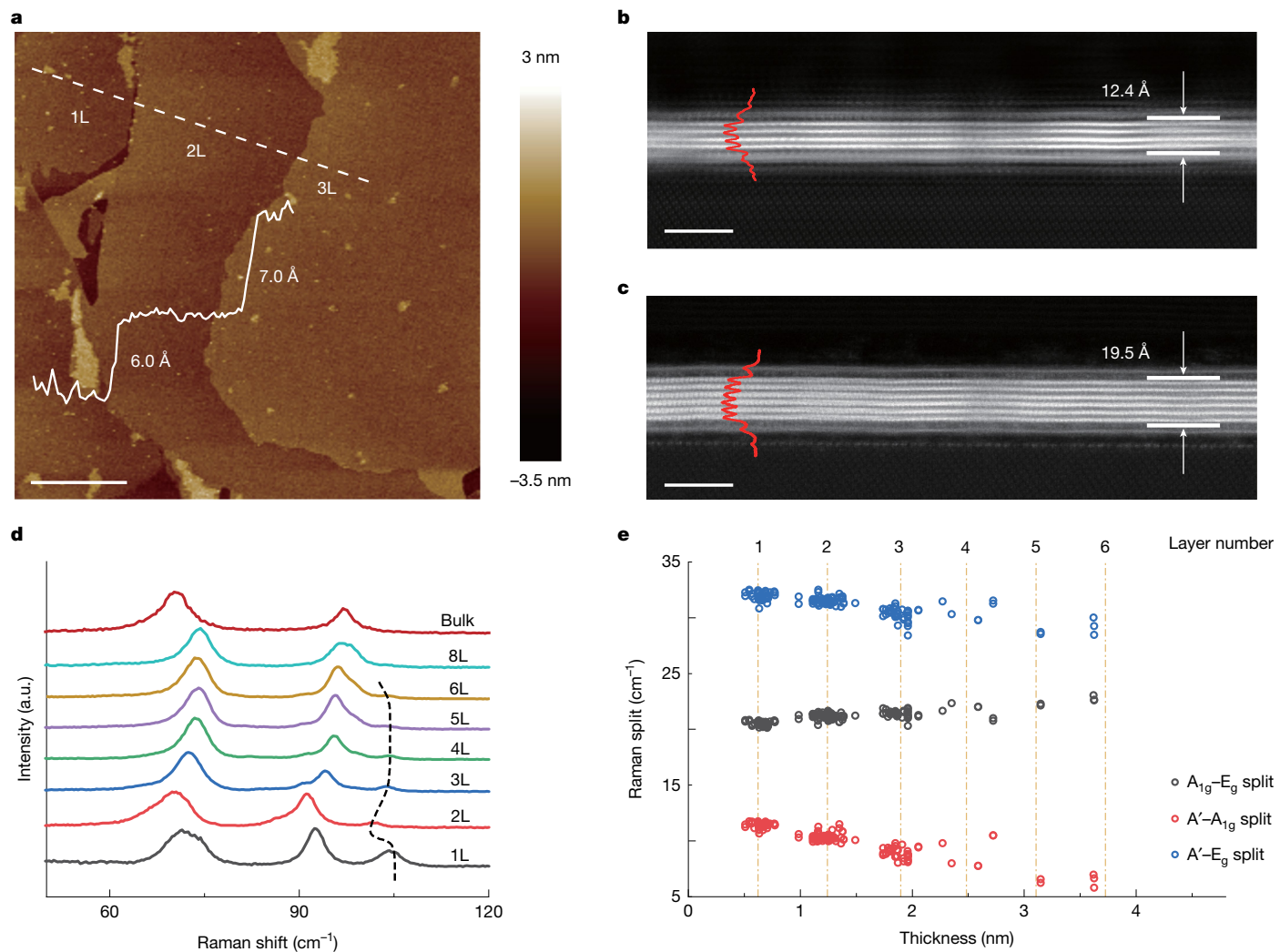


Fig. 4 | Layer-dependent properties. **a**, AFM image of a 2D Bi sample consisting of the monolayer, bilayer and trilayer Bi. The height profile along the white dashed line is marked. **b,c**, Cross-sectional view of HAADF-TEM images of a bilayer (**b**) and trilayer (**c**) Bi. **d**, Raman spectra of 2D Bi with different

thicknesses. **e**, Raman shift splitting of $A' - E_g$ (blue), $A' - A_{1g}$ (red) and $A_{1g} - E_g$ (black) against the 2D Bi thickness. a.u., arbitrary units. Scale bars, 1 μm (**a**) and 3 nm (**b,c**).

The longitudinal resistance versus temperature ($R_{xx}-T$) curve measured from a typical device is shown in Fig. 3b. At $T > 50$ K, R_{xx} of the monolayer Bi increases linearly with T , indicating a typically metallic behaviour dominated by electron–phonon scattering³⁰. The extracted electrical conductivity of monolayer Bi can reach $9.0 \times 10^6 \text{ S m}^{-1}$ at room temperature, an order of magnitude larger than the standard conductivity of Bi, that is, about $7.8 \times 10^5 \text{ S m}^{-1}$, most likely because of the single crystalline nature of monolayer Bi. The strongly enhanced electrical conductivity of Bi at its 2D limit might facilitate the possibility of various technological applications such as ultrathin interconnects. It is noteworthy that, although a recent study has demonstrated the electrical conductivity of thin layers of β -phase Bi, the thinnest thickness is limited to about 8 nm, far from the atomically thin limit⁹.

Being atomically thin, monolayer Bi is expected to exhibit notable electric field effects and possibly to be used in all-metallic transistors with superior performances^{10,16}. Figure 3c shows the dual sweep of longitudinal resistance R_{xx} as a function of top gate voltage V_{tg} for a typical monolayer device. A hole conduction behaviour is observed and further confirmed by Hall measurements (Extended Data Fig. 9). In contrast to bulk metals or semimetals in which the electric field effect is screened and therefore typically less than 1% (ref. 10) (Supplementary Fig. 7), monolayer Bi exhibits a notable electric field effect of about 35% by sweeping V_{tg} from -40 V to 40 V.

As discussed above, monolayer Bi is α -phase with the low symmetric C_{1h} point group; it may present excellent band geometric properties such as Berry curvature dipole (BCD)^{18,31}. Recent theoretical calculations indicate that α -phase monolayer Bi could host enhanced BCD and strong nonlinear Hall effect¹⁸. To confirm this, we perform nonlinear Hall measurements on monolayer Bi samples at 50 mK. From Fig. 3d, we can see that the nonlinear Hall voltage response $V_{xy}^{2\omega}$ scales linearly with the square of the driving current I_{xx}^ω , and reverses its sign when the driving current direction and the nonlinear Hall voltage probe connections are changed simultaneously, confirming the second-order nonlinear nature^{32–34}. Scaling law analysis suggests that the observed nonlinear Hall effect has the contribution from BCD^{32,35,36} (Supplementary Fig. 8). A nonlinear Hall conductivity $\sigma_{xy}^{2\omega} \approx 0.22 \mu\text{m V}^{-1}\Omega^{-1}$ is obtained (Methods). As shown by a benchmark comparison in Fig. 4d (inset), this $\sigma_{xy}^{2\omega}$ is giant, over two orders of magnitude larger than that in type-II Weyl semimetals (for example, WTe₂ and TaIrTe₄) and twisted bilayer MoS₂ (refs. 32–35,37,38).

Layer-dependent properties of Bi

Apart from the Bi monolayer, vdW squeezing methodology enables achievement of 2D Bi with various thicknesses (such as one-, two- and three-unit-cell thick) by adjusting the squeezing pressure (Extended

Data Fig. 10). Figure 4a–c shows typical AFM and cross-sectional STEM images of bilayer/trilayer samples (that is, two/three-unit-cell thick) with a corresponding thickness of about 12.4/19.5 Å (refer to quadrilayer, pentalayer and even thicker-layer 2D Bi in Supplementary Fig. 9).

Based on these samples, we thus study their layer-dependent properties. Figure 4d shows Raman spectra of 2D Bi at various thicknesses. Note that bulk Bi has two characteristic peaks at about 70.2 cm⁻¹ (E_g mode) and around 96.8 cm⁻¹ (A_{1g} mode)³⁹. An additional phonon mode at about 104 cm⁻¹ emerges in 2D Bi, which is particularly prominent in the monolayer case. This new phonon mode is confirmed by measurements under different excitation energies (Supplementary Fig. 11) and assigned to the A' mode by polarized Raman measurements (Supplementary Fig. 12). Notably, the new A' mode is strongly layer-dependent. When increasing the layer thicknesses, it shifts to the A_{1g} mode and diminishes in intensity gradually. In Fig. 4e, we plot the Raman shift splitting of $A' - E_g$, $A' - A_{1g}$ and $A_{1g} - E_g$ as a function of layer numbers. A linear relationship is found for all three cases, enabling the Raman spectroscopy an alternative to probe the layer number of 2D Bi.

Discussion and outlook

In conclusion, we demonstrate a simple, effective and universal vdW squeezing route towards 2D metals at the atomically thin limit by using two opposite ML-MoS₂/sapphire anvils. Various 2D metals, including Bi, Ga, In, Sn and Pb, are realized at the Å thickness limits. Owing to the complete encapsulation from the monolayer MoS₂, the as-produced 2D metals are environmentally stable and intrinsic, as confirmed by Bi, Sn, Pb samples (Supplementary Figs. 13–17). Notably, the encapsulated monolayer Bi can last for at least 1 year in our testing experiments. These 2D metals are cannot be easily separated from the MoS₂ encapsulation layers, if certain applications require the exposure of their surfaces. Taking 2D Bi as an example, we show many new physical properties that were previously not known. We foresee that this vdW squeezing technique would also offer an effective route for the implementation of 2D metal alloys and other diverse 2D non-vdW compounds^{40,41}, establishing a versatile material platform for the investigation of emerging quantum, electronic and photonic phenomena.

Online content

Any methods, additional references, Nature Portfolio reporting summaries, source data, extended data, supplementary information, acknowledgements, peer review information; details of author contributions and competing interests; and statements of data and code availability are available at <https://doi.org/10.1038/s41586-025-08711-x>.

1. Chen, Y. et al. Two-dimensional metal nanomaterials: synthesis, properties, and applications. *Chem. Rev.* **118**, 6409–6455 (2018).
2. Gou, J. et al. Two-dimensional ferroelectricity in a single-element bismuth monolayer. *Nature* **617**, 67–72 (2023).
3. Briggs, N. et al. Atomically thin half-van der Waals metals enabled by confinement heteroepitaxy. *Nat. Mater.* **19**, 637–643 (2020).
4. Xing, Y. et al. Quantum Griffiths singularity of superconductor-metal transition in Ga thin films. *Science* **350**, 542–545 (2015).
5. Jäck, B. et al. Observation of a Majorana zero mode in a topologically protected edge channel. *Science* **364**, 1255–1259 (2019).
6. Maniyara, R. A. et al. Tunable plasmons in ultrathin metal films. *Nat. Photon.* **13**, 328–333 (2019).
7. Zhu, F.-f. et al. Epitaxial growth of two-dimensional stanene. *Nat. Mater.* **14**, 1020–1025 (2015).
8. Ji, J. et al. Two-dimensional antimonene single crystals grown by van der Waals epitaxy. *Nat. Commun.* **7**, 13352 (2016).
9. Chen, L. et al. Exceptional electronic transport and quantum oscillations in thin bismuth crystals grown inside van der Waals materials. *Nat. Mater.* **23**, 741–746 (2024).
10. Novoselov, K. S. et al. Electric field effect in atomically thin carbon films. *Science* **306**, 666–669 (2004).
11. Geim, A. K. & Grigorieva, I. V. Van der Waals heterostructures. *Nature* **499**, 419–425 (2013).
12. Liu, Y. et al. Van der Waals heterostructures and devices. *Nat. Rev. Mater.* **1**, 16042 (2016).
13. Novoselov, K. S., Mishchenko, A., Carvalho, A. & Castro Neto, A. H. 2D materials and van der Waals heterostructures. *Science* **353**, aac9439 (2016).
14. Du, L. et al. Engineering symmetry breaking in 2D layered materials. *Nat. Rev. Phys.* **3**, 193–206 (2021).
15. Du, L. et al. Moiré photonics and optoelectronics. *Science* **379**, eadg0014 (2023).
16. Rotkin, S. V. & Hess, K. Possibility of a metallic field-effect transistor. *Appl. Phys. Lett.* **84**, 3139–3141 (2004).
17. Steves, M. A. et al. Unexpected near-infrared to visible nonlinear optical properties from 2-D polar metals. *Nano Lett.* **20**, 8312–8318 (2020).
18. Jin, K.-H., Oh, E., Stania, R., Liu, F. & Yeom, H. W. Enhanced Berry curvature dipole and persistent spin texture in the Bi(110) monolayer. *Nano Lett.* **21**, 9468–9475 (2021).
19. Reis, F. et al. Bismuthene on a SiC substrate: a candidate for a high-temperature quantum spin Hall material. *Science* **357**, 287–290 (2017).
20. Shao, Y. et al. Epitaxial growth of flat antimonene monolayer: a new honeycomb analogue of graphene. *Nano Lett.* **18**, 2133–2139 (2018).
21. Fang, A. et al. Bursting at the seams: rippled monolayer bismuth on NbSe₃. *Sci. Adv.* **4**, eaao0330 (2018).
22. Wu, X. et al. Epitaxial growth and air-stability of monolayer antimonene on PdTe₂. *Adv. Mater.* **29**, 1605407 (2017).
23. Huang, L. et al. Intercalation of metal islands and films at the interface of epitaxially grown graphene and Ru(0001) surfaces. *Appl. Phys. Lett.* **99**, 163107 (2011).
24. Calleja, F. et al. Spatial variation of a giant spin-orbit effect induces electron confinement in graphene on Pb islands. *Nat. Phys.* **11**, 43–47 (2014).
25. Hussain, N. et al. Ultrathin Bi nanosheets with superior photoluminescence. *Small* **13**, 1701349 (2017).
26. Li, L. et al. Epitaxy of wafer-scale single-crystal MoS₂ monolayer via buffer layer control. *Nat. Commun.* **15**, 1825 (2024).
27. Jiang, K. et al. Mechanical cleavage of non-van der Waals structures towards two-dimensional crystals. *Nat. Synth.* **2**, 58–66 (2023).
28. Singh, S. et al. Low-energy phases of Bi monolayer predicted by structure search in two dimensions. *J. Phys. Chem. Lett.* **10**, 7324–7332 (2019).
29. Lu, Y. et al. Topological properties determined by atomic buckling in self-assembled ultrathin Bi(110). *Nano Lett.* **15**, 80–87 (2015).
30. Kittel, C. & McEuen, P. *Introduction to Solid State Physics* (Wiley, 2018).
31. Sodemann, I. & Fu, L. Quantum nonlinear Hall effect induced by Berry curvature dipole in time-reversal invariant materials. *Phys. Rev. Lett.* **115**, 216806 (2015).
32. Kang, K., Li, T., Sohn, E., Shan, J. & Mak, K. F. Nonlinear anomalous Hall effect in few-layer WTe₂. *Nat. Mater.* **18**, 324–328 (2019).
33. Ma, Q. et al. Observation of the nonlinear Hall effect under time-reversal-symmetric conditions. *Nature* **565**, 337–342 (2019).
34. Wu, F. et al. Giant correlated gap and possible room-temperature correlated states in twisted bilayer MoS₂. *Phys. Rev. Lett.* **131**, 256201 (2023).
35. Ma, T. et al. Growth of bilayer MoTe₂ single crystals with strong non-linear Hall effect. *Nat. Commun.* **13**, 5465 (2022).
36. Du, L. et al. Nonlinear physics of moiré superlattices. *Nat. Mater.* **23**, 1179–1192 (2024).
37. Kumar, D. et al. Room-temperature nonlinear Hall effect and wireless radiofrequency rectification in Weyl semimetal TaIrTe₄. *Nat. Nanotechnol.* **16**, 421–425 (2021).
38. Huang, M. et al. Giant nonlinear Hall effect in twisted bilayer WSe₂. *Natl. Sci. Rev.* **10**, nwac232 (2022).
39. Lannin, J. S., Calleja, J. M. & Cardona, M. Second-order Raman scattering in the group-V_b semimetals: Bi, Sb, and As. *Phys. Rev. B* **12**, 585–593 (1975).
40. Puthirath Balan, A. et al. Exfoliation of a non-van der Waals material from iron ore hematite. *Nat. Nanotechnol.* **13**, 602–609 (2018).
41. Balan, A. P. et al. Non-van der Waals quasi-2D materials; recent advances in synthesis, emergent properties and applications. *Mater. Today* **58**, 164–200 (2022).

Publisher's note Springer Nature remains neutral with regard to jurisdictional claims in published maps and institutional affiliations.

Springer Nature or its licensor (e.g. a society or other partner) holds exclusive rights to this article under a publishing agreement with the author(s) or other rightsholder(s); author self-archiving of the accepted manuscript version of this article is solely governed by the terms of such publishing agreement and applicable law.

© The Author(s), under exclusive licence to Springer Nature Limited 2025

Methods

Growth of MoS₂ on sapphire

Monolayer MoS₂ is epitaxially grown on *c*-plane sapphire (2-inch wafer) by chemical vapour deposition. The sulfur (Alfa Aesar, 99.9%, 6 g) and MoO₃ (Alfa Aesar, 99.999%) powders are used as precursors. During the growth, sulfur source, MoO₃ source and sapphire substrate are at about 120 °C, 560 °C and 880 °C, respectively. The growth lasts for around 40 min for full coverage. For vdW squeezing experiments, MoS₂/sapphire samples are cut into approximately 1-cm² large square pieces, acting as anvils.

vdW squeezing of 2D metals

Metals tested in this study are Bi (99.9999%), Ga (99.99999%), In (99.99995%), Sn (99.9999%) and Pb (99.999%) from ZhongNuo Advanced Material Technology. The whole vdW squeezing process is performed inside in a glove box with a water/oxygen concentration of less than 0.1 ppm. The operating apparatus mainly consists of a bottom/top plate, bottom/top heat shield and press components. Note that the bottom/top plate (made of tungsten steel) can be heated up to 500 °C at the maximum and exert force up to 50,000 N at the maximum. When squeezing, the anvils/metal assembly is placed between the two plates. During squeezing, the temperatures are 280 °C, 100 °C, 180 °C, 400 °C and 340 °C for Bi, Ga, In, Sn and Pb, respectively. The pressure exerted on the two opposite anvils by a custom-made presser is about 140 MPa, 120 MPa, 130 MPa, 130 MPa and 150 MPa for Bi, Ga, In, Sn and Pb, respectively. The samples are cooled down while maintaining the squeezing pressure constant. The cooling process is maintained at a slow rate and typically lasts for 4 h from about 300 °C to room temperature.

Sample characterizations

Optical microscopy images are taken using MM-400, Nikon. AFM imaging is performed by Bruker Icon and Bruker Multimode 8. Raman spectra are acquired by Horiba Raman spectroscopy (LabRam HR Evolution) in a confocal backscattering geometry (confocal pinhole of 100 μm). The laser power during measurements is kept at less than 350 μW to avoid sample damage and excessive heating. SAED is performed in a TEM (JEM-F200, JEOL) operating at 200 kV. Atomic-resolution HAADF-STEM images are acquired by an aberration-corrected spectrum 300 TEM (ThermoFisher) operating at 300 kV. EDS was acquired by spectra 300 TEM. In-plane XRD measurements are performed by a Rigaku SmartLab X-Ray Diffractometer with an in-plane arm. The X-ray is generated by a rotating anode source with a power of about 9 kW and a wavelength of around 1.541 Å.

Device fabrication

The devices in the Hall bar geometry are directly fabricated on the anvil. The MoS₂/Bi/MoS₂ samples on sapphire are first isolated by scratching off their surrounding materials with a tungsten tip. Then the devices are fabricated by the standard micro-fabrication processes, including laser or e-beam lithography, reactive ion etching, metal evaporation and lifting-off. Contact electrodes are Au (about 15 nm), and hBN flake (30–80 nm) transferred on top of MoS₂ by dry transfer technique is used as the gate dielectric layer. Gate electrodes are Au (30 nm) deposited on hBN.

Transport measurements

The transport measurements are performed in two cryogenic systems: Model C-Mag Vari-9T Research System (CRYOMAGNETICS) with a

base temperature of 1.5 K and CF-CS81 system (Leiden Cryogenics BV) with a base temperature of 20 mK. Lock-in amplifiers (SR830), Source-Meters (Keithley 2400) and multimeters (DMM 7510) are used for the measurements.

Nonlinear Hall conductivity

In general, the current density of nonlinear Hall effect driven by an electric field E_{xx}^ω with oscillating frequency ω can be written as $j_{xy}^{2\omega} = \sigma_{xy}^{2\omega}(E_{xx}^\omega)^2$, where $\sigma_{xy}^{2\omega}$ is the nonlinear Hall conductivity. The nonlinear Hall current response generates the electric field of frequency 2ω , given by $j_{xy}^{2\omega} = \sigma_0 E_{xy}^{2\omega}$, where σ_0 is the linear conductivity. Considering that longitudinal voltage $V_{xx}^\omega = E_{xx}^\omega L$ and nonlinear Hall voltage $V_{xy}^{2\omega} = E_{xy}^{2\omega} W$, we obtain $\sigma_{xy}^{2\omega} = \sigma_0 \frac{V_{xy}^{2\omega} L^2}{(V_{xx}^\omega)^2 W}$, where L is the device channel length and W is the width.

Theoretical calculations

Density functional theory calculations are performed using the Vienna Ab-initio Simulation Package⁴² with the projector-augmented wave pseudopotentials⁴³. The Perdew–Burke–Ernzerhof version of the generalized gradient approximation is used for the exchange-correlation functional⁴⁴. DFT-D3 is used to correct the weak vdW interaction between MoS₂ and Bi layers⁴⁵.

Data availability

Source data are provided with this paper. The datasets used for Figs. 3 and 4 and Extended Data Figs. 5, 7 and 9 are provided as Source data. All other data are available from the corresponding authors upon request.

- 42. Kresse, G. & Furthmüller, J. Efficient iterative schemes for *ab initio* total-energy calculations using a plane-wave basis set. *Phys. Rev. B* **54**, 11169–11186 (1996).
- 43. Kresse, G. & Joubert, D. From ultrasoft pseudopotentials to the projector augmented-wave method. *Phys. Rev. B* **59**, 1758–1775 (1999).
- 44. Perdew, J. P., Burke, K. & Ernzerhof, M. Generalized gradient approximation made simple. *Phys. Rev. Lett.* **77**, 3865–3868 (1996).
- 45. Grimme, S., Antony, J., Ehrlich, S. & Krieg, H. A consistent and accurate *ab initio* parametrization of density functional dispersion correction (DFT-D) for the 94 elements H–Pu. *J. Chem. Phys.* **132**, 154104 (2010).

Acknowledgements We thank N. Lu, M. Zhu and L. Yang for their assistance with the in-plane XRD measurements. We thank X. Li for the SAED analysis and Y. Wang for the discussions. This work is supported by the National Key Research and Development Program of China (grant no. 2021YFA1202900), the National Natural Science Foundation of China (NSFC, grants 62488201, 12422402, 12274447 and 62204166), the Guangdong Major Project of Basic and Applied Basic Research (2021B0301030002) and the China National Postdoctoral Program for Innovative Talents (no. BX20230251). L. Du acknowledges the National Key R&D Program of China (grant 2023YFA1407000).

Author contributions G.Z. proposed and supervised the project; J.Z. was involved in all aspects of this work, including experimental setup, sample preparations and electrical and optical characterizations with help from J.D., K.J., X.L., Z.H., J. Liu, Y.C., X.Z. and S.W.; P.L., J.P. and S.D. conducted the theoretical calculations. L. Dai took the in-plane XRD measurements; Y.W. and P.Z. prepared the fast-cooling samples; L.L., L.Z., Y.Z., H.Y., Z.W., J. Li and B.W. provided the MoS₂/sapphire samples; J.Z., L. Du, W.Y. and G.Z. analysed the data with help from N.L. and D.S.; and J.Z., L. Du and G.Z. wrote the paper with the input from all authors.

Competing interests The authors declare no competing interests.

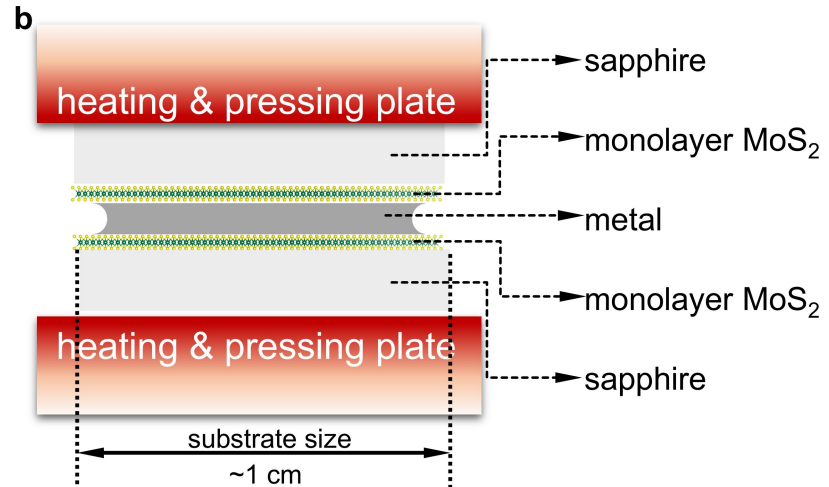
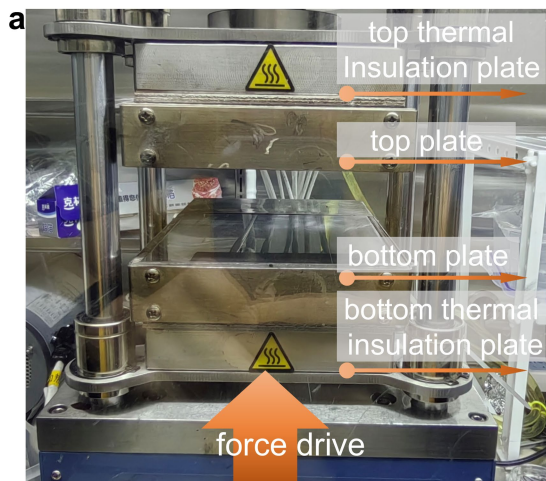
Additional information

Supplementary information The online version contains supplementary material available at <https://doi.org/10.1038/s41586-025-08711-x>.

Correspondence and requests for materials should be addressed to Luojun Du or Guangyu Zhang.

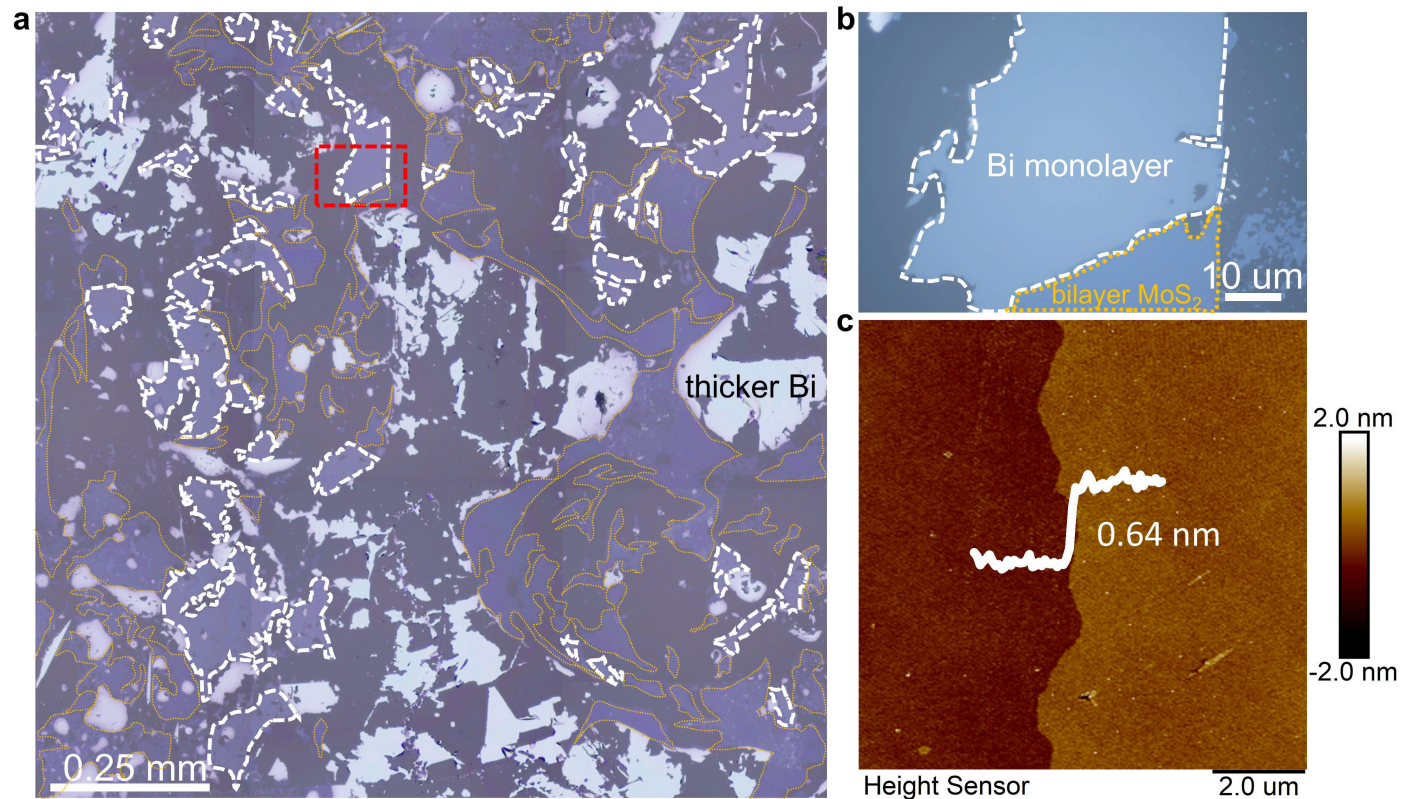
Peer review information *Nature* thanks Fengxia Geng, Han Woong Yeom and the other, anonymous, reviewer(s) for their contribution to the peer review of this work. Peer reviewer reports are available.

Reprints and permissions information is available at <http://www.nature.com/reprints>.



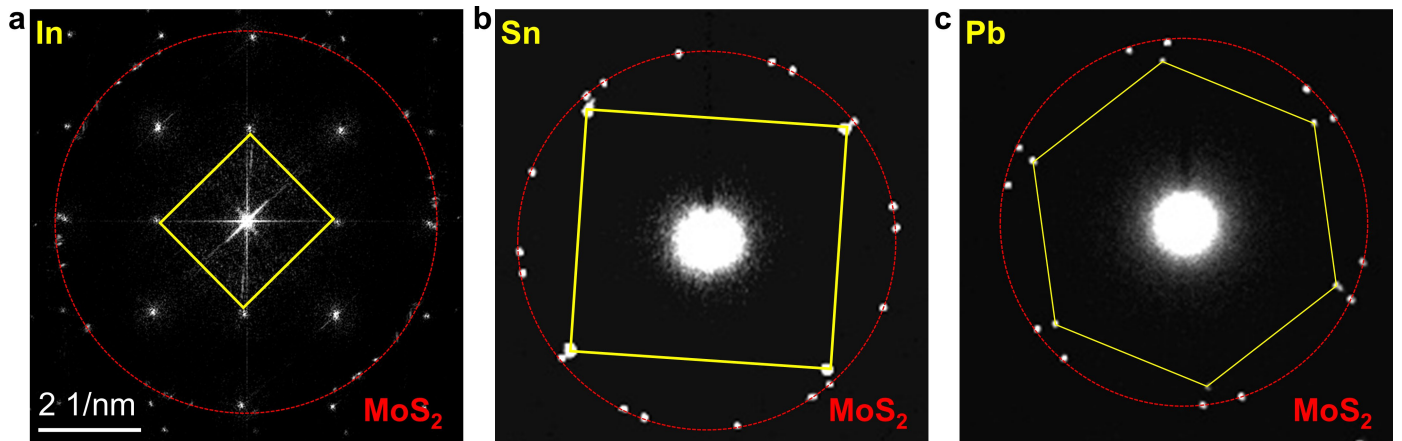
Extended Data Fig. 1 | The photograph and diagram of the squeezing setup. Note that the bottom/top plate (made of tungsten steel) can be heated up (temperature range: 20–500 °C) and exerted force (force range: 0–50000 N).

Article



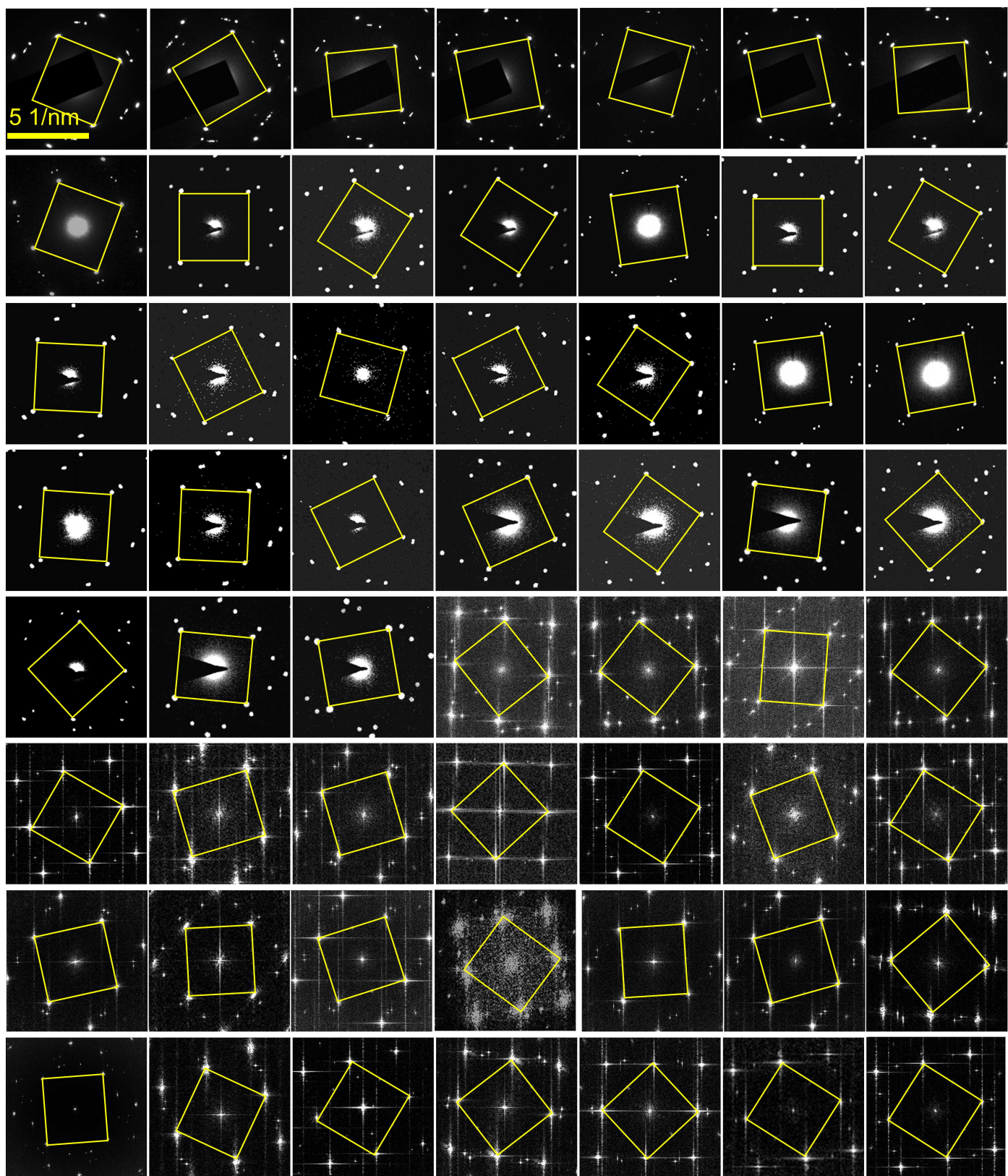
Extended Data Fig. 2 | The large-scale optical image. **a**, The optical microscopy images of Bi over a $\sim 1 \text{ mm}^2$ area produced under $\sim 140 \text{ MPa}$. Those areas marked with white dashed lines are the monolayer regions; while those areas marked with brown dashed lines are the bilayer MoS_2 regions without

metal inside. **b**, Zoom-in optical images taken from the red rectangular area of (a). **c**, AFM images of monolayer Bi. The height line profile indicates the thickness of $\sim 0.64 \text{ nm}$.

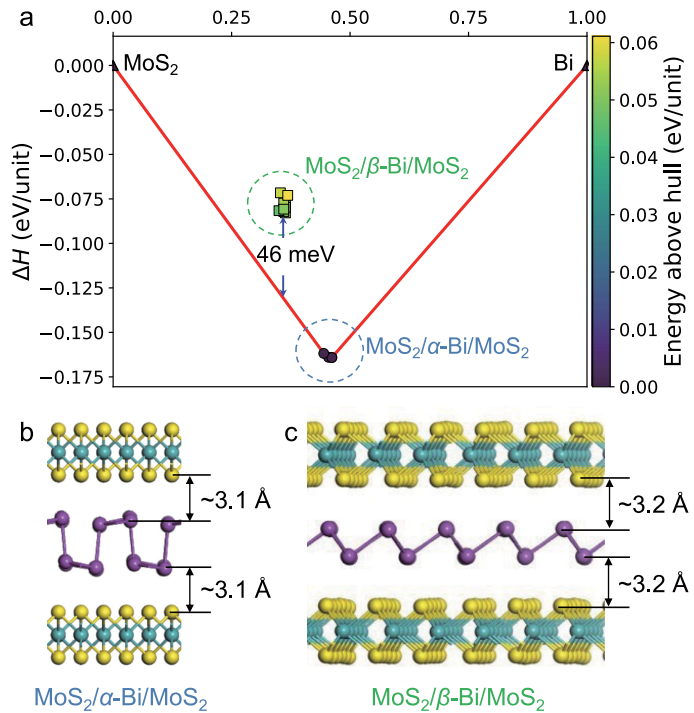


Extended Data Fig. 3 | The diffraction patterns of In (a), Sn (b), and Pb (c). In addition to the diffraction spots from MoS₂ (marked in red), sharp and regular diffraction spots (marked in yellow) can be recognized explicitly for In, Sn and

Pb, suggesting the single crystal nature. From the diffraction patterns, we can extract that In and Sn have a rectangle lattice structure, while Pb has a hexagonal lattice structure.

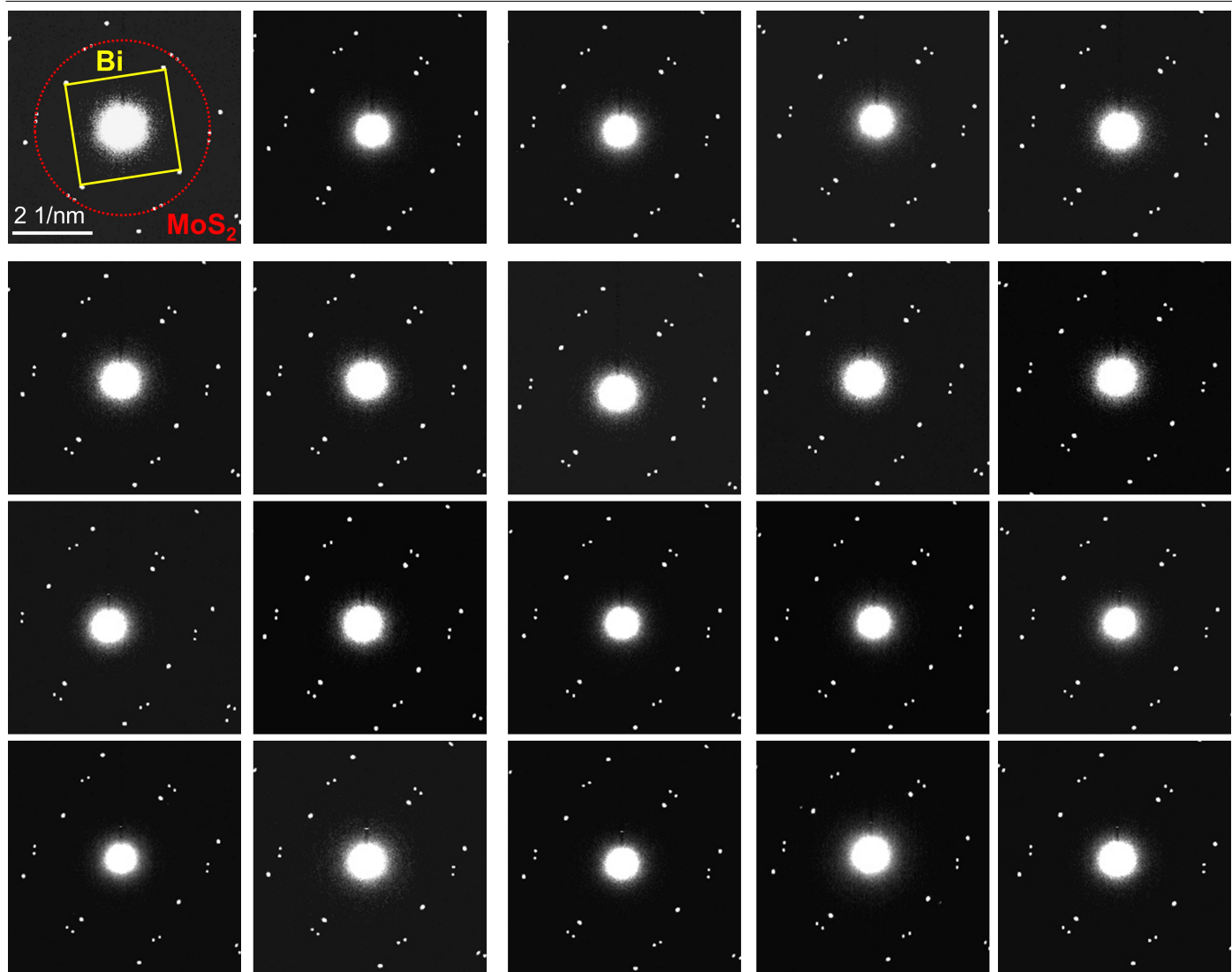


Extended Data Fig. 4 | The diffraction patterns taken from 56 monolayer Bi samples. All the monolayer Bi samples show rectangle diffraction patterns and thus are α -phase.



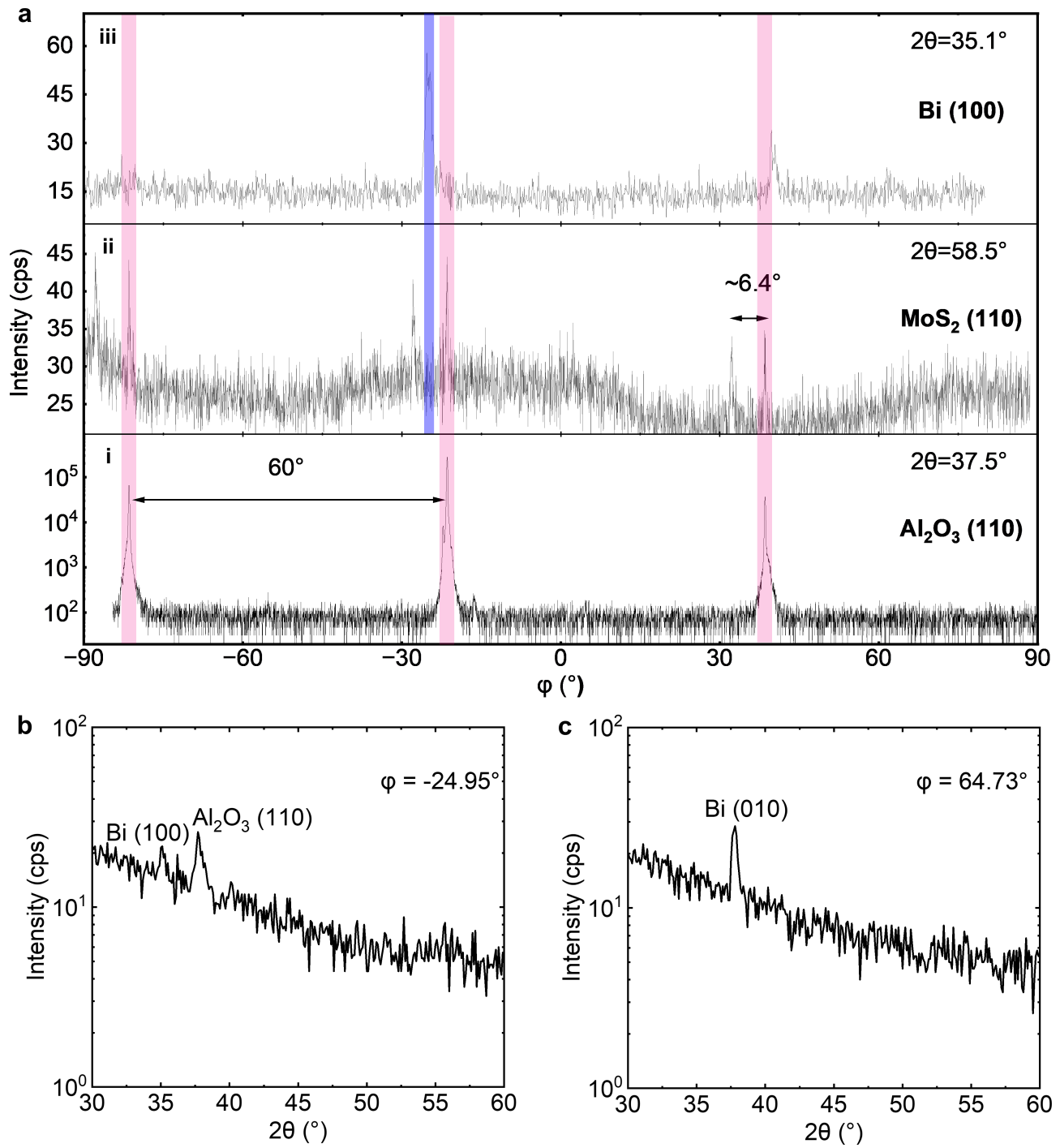
Extended Data Fig. 5 | Theoretical calculations. **a.** Formation enthalpies ΔH of the selected configurations. The magnitude of the energy above hull is represented by colour, as indicated by the colour bar. **b,c.** The schematic diagrams of heterojunctions composed of α -Bi(110) (b) and β -Bi(111) (c). Both the formation enthalpies ΔH and the energy above convex hull for MoS₂/ α -Bi/MoS₂ are lower than those for MoS₂/ β -Bi/MoS₂, indicating that the α phase structure is more energy favourable and thus the ground state phase. In addition, the interlayer spacing between α -Bi and MoS₂ is -3.1 Å, which signifies the vdW stacking.

Article



Extended Data Fig. 6 | SAED patterns taken from randomly picked 20 positions across the entire Bi film. The diffraction area is -1 μm, and adjacent SAED patterns are taken more than 5 μm apart. It can be seen that these SAED

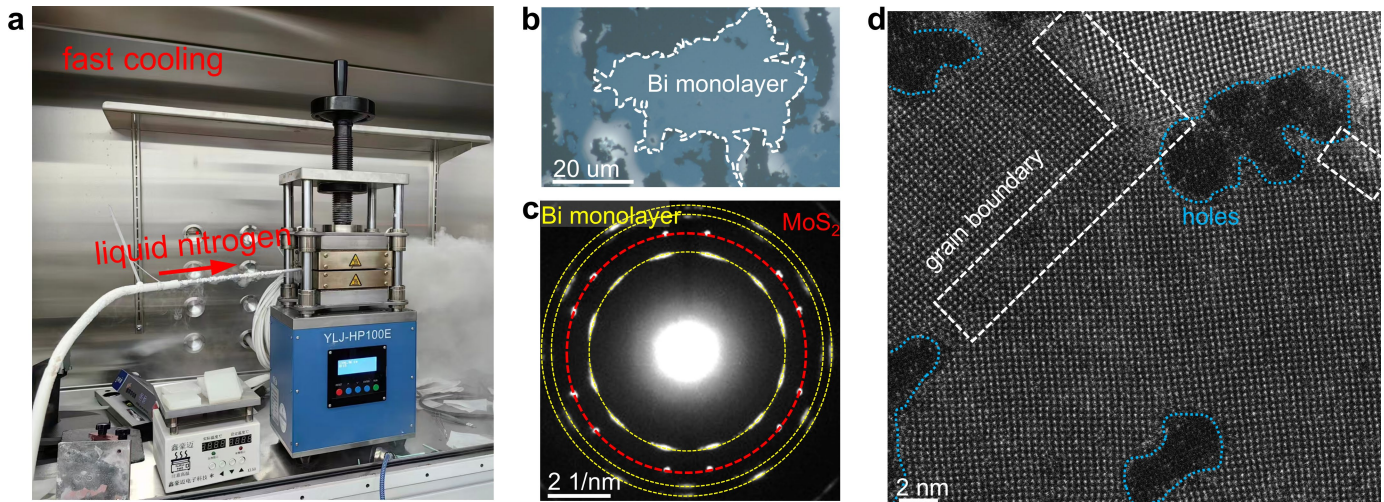
patterns are essentially identical with a degree of rotational misalignment <1°, evidencing the single-crystalline nature of the achieved monolayer Bi.



Extended Data Fig. 7 | In-plane XRD measurements. **a**, XRD pattern of φ scan using Al_2O_3 (110), MoS_2 (110), and Bi (100) Bragg condition respectively. **b,c**, XRD pattern of an in-plane scan around the Bi (100) Bragg condition (b)

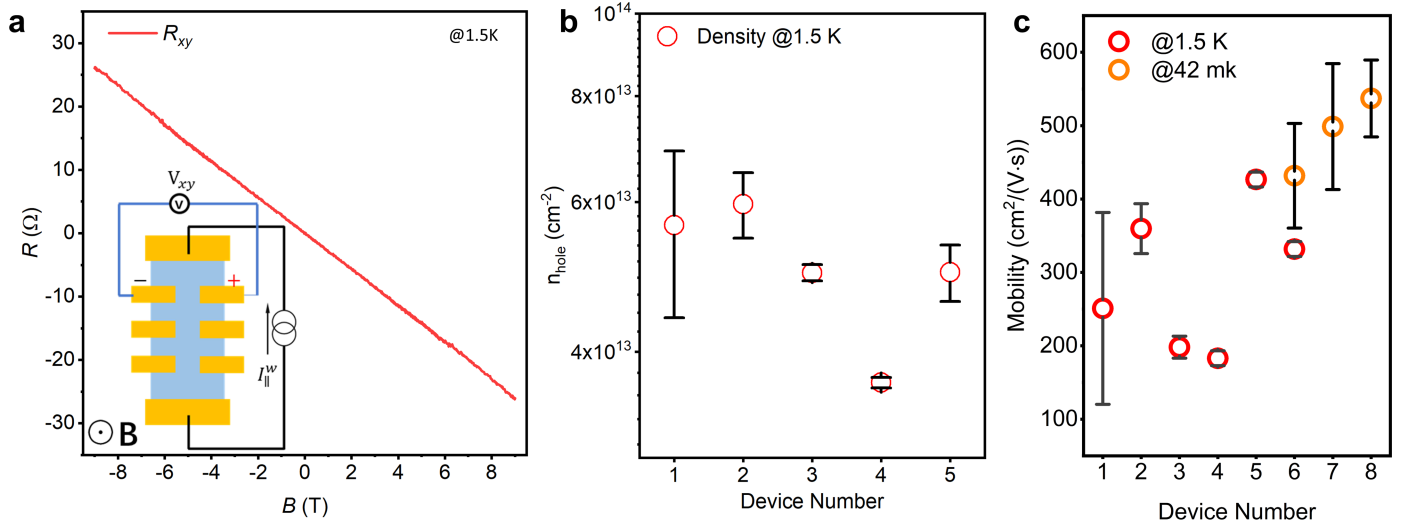
and around the Bi (010) Bragg condition (c). The 2θ angle of $35.104^\circ \pm 0.045^\circ$ ($37.764 \pm 0.013^\circ$) indicates the lattice parameter of monolayer Bi $5.108 \pm 0.006 \text{ \AA}$ ($4.760 \pm 0.001 \text{ \AA}$), which matches well with the measured TEM results.

Article



Extended Data Fig. 8 | vDW squeezing experiments under the fast-cooling process. **a**, The photograph of the operating apparatus for the fast-cooling process. Cryogenic nitrogen (from a liquid nitrogen tank) is aggressively blown to the sample for the fast-cooling process. In such way, the samples can cool down quickly within 10 min. **b-d**, The optical image, SAED pattern,

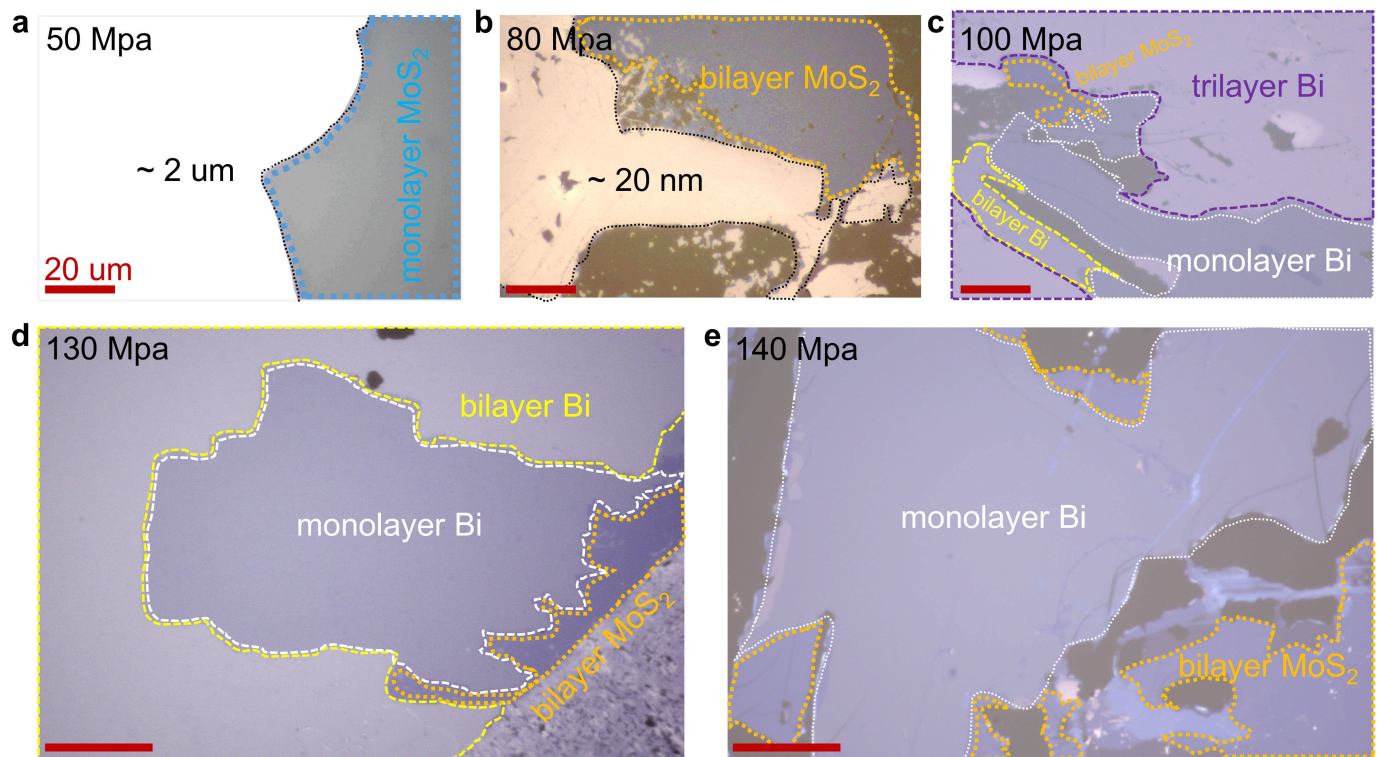
atomic-resolution STEM image of the as-produced Bi under the fast-cooling process. Monolayer Bi can be reliably achieved, but with much smaller grain sizes and some grain boundaries can be clearly seen at the grain-grain jointing regions. It is noteworthy that from the atomic-resolution STEM image, the as-produced Bi under the fast-cooling process is also α -phase.



Extended Data Fig. 9 | Hall measurements. **a**, Antisymmetrized Hall resistance versus the magnetic field from -9 T to 9 T. The inset is the measurement configuration. The sign of Hall voltage demonstrates the *p*-type behavior of 2D-Bi film. **b**, Carrier density extracted from Hall measurements

across several samples. **c**, The extracted Hall mobility of monolayer Bi at 1.5 K and 42 mK from different devices. At 1.5 K (42 mK), the average Hall mobility of monolayer Bi is ~ 300 $\text{cm}^2\text{V}^{-1}\text{s}^{-1}$ (~ 500 $\text{cm}^2\text{V}^{-1}\text{s}^{-1}$). The extracted mean free path is ~ 100 nm.

Article



Extended Data Fig. 10 | vdW squeezing experiments under different pressures. The optical microscope images of the as-produced Bi under 50 MPa (a), 80 MPa (b), 100 MPa (c), 130 MPa (d), 140 MPa (e). The scale bars are 20 μm . When the applied pressure is small, i.e., 50 MPa and 80 MPa, all Bi samples produced are thick and no monolayer Bi can be found. When the applied

pressure is increased to a moderate value, i.e., 100 MPa and 120 MPa, mono-, bi-, tri-, and few-layer Bi samples can be observed simultaneously, and the probability that monolayer Bi occurs increases with increasing the applied pressure. When the applied pressure is high, i.e., 140 MPa, Bi monolayers larger than 100 μm can be obtained.